SAND2020-7018C

**Proceedings of the ASME 2020
Internal Combustion Engine Division Fall Technical Conference
ICEF2020
November 1-4, 2020, Denver, CO, USA**

ICEF2020-3003

LARGE EDDY SIMULATION OF LEAN MIXED-MODE COMBUSTION ASSISTED BY PARTIAL FUEL STRATIFICATION IN A SPARK-IGNITION ENGINE

Chao Xu[*], **Sibendu Som**
Argonne National Laboratory
Lemont, IL

Magnus Sjöberg
Sandia National Laboratories
Livermore, CA

ABSTRACT

Lean operation is beneficial to spark-ignition engines due to the high thermal efficiency compared with conventional stoichiometric operation. Lean combustion can be significantly stabilized by the partial fuel stratification (PFS) strategy, in which a small amount of pilot injection is applied near the spark energizing timing in addition to main injections during intake. Furthermore, mixed-mode combustion, which makes use of end-gas autoignition following conventional deflagration-based combustion, can be further utilized to speed up the overall combustion. In this study, PFS-assisted mixed-mode combustion in a lean-burn direct injection spark-ignition (DISI) engine is numerically investigated using multi-cycle large eddy simulation (LES). To accurately represent the pilot injection characteristics, experimentally-derived spray morphology parameters are employed for spray modeling. A previously developed hybrid G-equation/well-stirred reactor model is extended to PFS conditions, to capture interactions of pilot injection, turbulent flame propagation and end-gas autoignition. The LES-based engine model is compared with Reynolds-averaged Navier-Stokes (RANS) based model, allowing an investigation of both mean and cycle-to-cycle variation (CCV) of combustion characteristics. Instantaneous spray and flame structures from simulations are compared with experiments. The LES-based model is finally leveraged to investigate impacts of fuel properties including heat of vaporization (HoV) and laminar flame speed (S_L). It is shown that overall, the predicted mean pressure and heat release rate traces from both RANS and LES agree well with the experiment, while LES captures the CCV and the combustion phasing in the mass burned space much better than RANS. Predicted liquid fuel penetrations agree reasonably well with the experiment, both for RANS and LES. Detailed flame structures in the simulations also reveal the transition from a sooting flame to a lean premixed flame, which is consistent with experimental findings. LES is shown to capture more wrinkled and stretched flame fronts than RANS. Local sensitivity analysis further identifies the stronger combustion phasing sensitivity to S_L compared with that to HoV, and the stronger sensitivity of autoignition heat release rate than deflagration. The results from this study demonstrate the high fidelity of the developed computational model based on LES, enabling future investigation of PFS-assisted mixed-mode combustion for different fuels and a wider range of operating conditions.

Keywords: spark-ignition engine, mixed-mode combustion, partial fuel stratification, large eddy simulation, fuel property sensitivity

NOMENCLATURE

γ	Residual gas fraction
μ	Molecular viscosity
μ_T	Turbulent viscosity
ϕ	Equivalence ratio
ρ	Density
$\tilde{G}''$	Mean variance of signed distance to turbulent flame
$\tilde{G}$	Mean signed distance to the mean turbulent flame
ξ	Burned mass fraction
D_T	Turbulent diffusivity
Da	Damköhler number

---

[*] Contact author: chaoxu@anl.gov

Sandia National Laboratories is a multimission laboratory managed and operated by National Technology & Engineering Solutions of Sandia, LLC, a wholly owned subsidiary of Honeywell International Inc., for the U.S. Department of Energy's National Nuclear Security Administration under contract DE-NA0003525.

p	Pressure
P_{max}	Peak cylinder pressure
S_L	Laminar flame speed
S_T	Turbulent flame speed
T_0	Unburned temperature
u'	Turbulent velocity
AHRR	Apparent heat release rate
CA	Crank angle
CCV	Cycle-to-cycle variation
CFD	Computational fluid dynamics
CoV	Coefficient of variation
EGR	Exhaust gas recirculation
HoV	Heat of vaporization
IMEP	Indicated mean effective pressure
IVC	Intake valve closing
LES	Large eddy simulation
MON	Motor octane number
PFS	Partial fuel stratification
RANS	Reynolds-averaged Navier-Stokes
RON	Research octane number
SACI	Spark-assisted compression ignition
SPCCI	Spark plug controlled compression ignition
TDC	Top dead center

1 INTRODUCTION

With the increasing demand in global energy supplies and stringent emission regulations, cleaner and more efficient engine combustion technologies remain to be developed [1]. Lean operation can provide high thermal efficiency compared with conventional stoichiometric operation [2]. However, operation with early injections creates a near-homogeneous lean mixture which is prone to excessive cycle-to-cycle variations (CCV) due to a reduced flame speed and hence an increased importance of flame-flow interactions. Partial fuel stratification (PFS) is a promising strategy to improve the stability for lean combustion by stabilizing the spark-initiated deflagration [3]. In PFS, in addition to the early injections during the intake stroke, a fraction of fuel, referred to as pilot injection, is injected concurrently with the spark-ignition, thus creating a partially stratified local mixture which enables stable deflagrative combustion. However, relying only on deflagration is insufficient for ultra-lean operation because of an excessively long burn duration. To overcome this challenge, mixed-mode combustion, or spark-assisted compression ignition (SACI), can be further utilized to speed up the overall combustion whereby a portion of the charge is consumed via normal deflagration and the remainder via autoignition of the end-gas. Therefore, PFS-assisted lean mixed-mode combustion is an emerging advanced engine combustion technology featuring high efficiency, low emission, and stable operation at the same time, and a similar technology, namely Spark Plug Controlled Compression Ignition (SPCCI), has been demonstrated in the Mazda's Skyactive-X Engine [4].

The performance and operability of the PFS-assisted lean mixed-mode engine operation depend on a variety of in-cylinder processes, including pilot injection, flame kernel initiation and development, and end-gas autoignition. For example, the local mixture stratification near the spark has a strong implications on ignition reliability, the initial speed of flame kernel development, as well as soot emission [3]. The rate of flame propagation determines the onset of end-gas autoignition, while the heat release rate due to autoignition is largely affected by temperature and mixture stratification in the end-gas [5,6]. All of these processes actively interact with, or may even be controlled by, the complex flow patterns in a turbulent environment. Provided with such tight couplings of spray and spark, and of deflagration and autoignition, understanding the detailed physics involved in these processes is key to improving in combustion control for the PFS-assisted lean mixed-mode engine operation.

On the other hand, the performance of an SI engine can strongly depend on the fuel being used, or more particularly, the physical and chemical properties of the fuels. For conventional stoichiometric boosted SI engine operation, impacts of different fuel properties have been systematically investigated in the literature [7, 8, 9, 10]. A recent report from U.S. Department of Energy presented an engine efficiency merit function correlated with fuel properties, based on the experimental data from various sources [11]. The merit function identified positive correlations between the efficiency gain and key fuel properties, such as the Research Octane Number (RON), octane sensitivity S ($S = RON - MON$, MON is Motor Octane Number), heat of vaporization (HoV) and laminar flame speed (S_L), either through knock mitigation or higher exhaust gas recirculation (EGR)-dilution potential. These observed fuel property impacts, however, are limited to the stoichiometric EGR-dilute boosted-SI operation, and the extension to the mixed-mode operation is not straightforward.

High-fidelity computational fluid dynamics (CFD) simulations provide a powerful tool to enable full three-dimensional (3D) access to all physical and chemical processes in a time-resolved fashion, and to allow isolated investigations of fuel property impacts, both of which are challenging using experiments. For example, CFD simulations have been used in previous studies to investigate SACI combustion using Reynolds-averaged Navier Stokes (RANS) [12, 13, 14, 15] or large eddy simulation (LES) [16, 17] based models. In these previous studies, RANS-based models, in general, were able to capture the mean combustion characteristics, while LES-based models further showed the capability of predicting CCV [14]. However, very few numerical studies have been focused on the PFS-assisted lean SACI operation.

In this study, an LES-based CFD model for multi-cycle engine simulations of PFS-assisted SACI is presented. The previously developed RANS model targeting the well-mixed charge operation [15] is extended to account for pilot injection and to couple LES for more accurate spray and flame characterizations. The model will be validated extensively against experimental data on crank-angle resolved pressure traces and in-cylinder spray and flame imaging. The multi-cycle LES model will also be compared with the widely-used RANS model. The validated multi-cycle LES model will then be leveraged to provide detailed characterization of spray and flame structures, as well as mixture inhomogeneity, and to investigate impacts of fuel properties on PFS-assisted SACI combustion features for future optimization of fuels and engines. To the authors' best knowledge, this is the first multi-cycle LES study for the PFS-assisted SACI engine operation.

2 EXPERIMENTAL AND NUMERICAL CONFIGURATIONS

2.1 Experimental Setup

The experiments were performed in a single-cylinder, four-valve, direct-injection spark-ignition (DISI) research engine operated at Sandia National Laboratories. Figure 1 shows a cross-sectional view of the combustion chamber at top dead center (TDC). One of the intake valves was deactivated to enhance the in-cylinder swirl level and thereby the overall mixing process. The engine can be set up in two configurations, i.e., an optical configuration and an all-metal configuration. The two configurations are nearly identical except that the optical engine has quartz windows in the pent-roof and piston to provide optical access to in-cylinder spray and combustion processes, while all-metal piston and metal blank in the pent-roof were used to enable continuously fired all-metal engine experiments. In this study, the former was employed to provide spray and flame imaging for model validation and enhancement.

A certification gasoline blended with 30% ethanol by volume (referred to as E30 hereinafter) was used in the experiments. The E30 fuel has RON and MON of 105 and 91, respectively. Fuel can be directly injected into the combustion chamber during the intake stroke to generate a well-mixed charge, or during the compression stroke to generate a stratified charge. In this study, a combined injection strategy, i.e., PFS, was employed: triple early injections to provide a lean background mixture with an equivalence ratio (ϕ) of 0.48, and a late pilot injection to create localized fuel stratification near spark timing resulting in a global ϕ of 0.5. Compared with the well-mixed charge engine operation, PFS has proven to have supreme controls on the start of combustion (SoC) [3] and to maintain a low level of CCV. Engine specifications and key PFS engine operation parameters are provided in Table 1. For more details on engine operation strategies, readers are referred to Ref. [3].

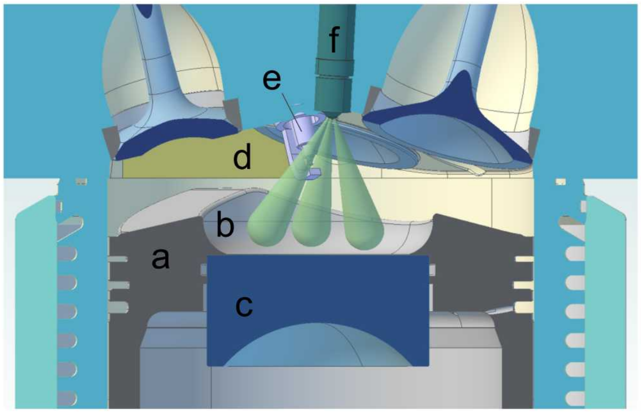

FIGURE 1: Cross-sectional engine schematic at TDC: a-Piston; b-Piston bowl; c-Piston bowl window; d-Pent-roof quartz window; e-Spark plug; f-Fuel injector.

2.2 Numerical Methodology

The simulations are performed using the CONVERGE code v2.4 [18] on a full-scale engine geometry shown in Fig. 2. The code features second-order accuracy for spatial discretization and first-order accuracy for time integration. The computational domain contains intake and exhaust ports and valves, cylinder, spark plug, and fuel injector. Crank-angle resolve pressure measurements at the intake port inlet and the exhaust port outlet are taken as boundary conditions for simulations. The liquid spray and gas-phase combustion are solved with the Eulerian-Lagrangian approach. Droplet breakup, evaporation, and drag are modeled with the Kelvin-Helmholtz and Rayleigh-Taylor model [19], the Frossling correlation [20], and dynamic drag model [21], respectively. Wall heat transfer is modeled with a temperature wall function [22]. Temperature of the cylinder walls is specified as 435 K. The dynamic structure LES model [23] is employed in this study and its performance is further compared with RANS simulations based on the re-normalized group (RNG) $k-\varepsilon$ model. Note that one focus of this study is to demonstrate the improved fidelity of the multi-cycle LES model compared with the conventionally used RANS model.

A hybrid level-set G-equation/well-stirred reactor model [24] is used to model turbulent combustion associated with both flame propagation and end-gas autoignition. In the G-equation model, turbulent flame propagation is governed by a transport equation of a passive scalar G [25],

$$\bar{\rho}\partial_t\tilde{G}+\bar{\rho}\tilde{\boldsymbol{u}}\cdot\nabla\tilde{G}=-\bar{\rho}\tilde{D_T}\tilde{\kappa}|\nabla\tilde{G}|+\widetilde{\rho_u S_T}|\nabla\tilde{G}|, \tag{1}$$

with the two right-hand-side terms representing the curvature effect and turbulent flame front propagation, respectively. Symbol "$\sim$" indicates the Favre-averaged mean in RANS and the Favre-filtered quantity in LES. ρ is density, $\boldsymbol{u}$ is the velocity vector, D_T

TABLE 1: Engine specifications and PFS operating condition.

Engine specification	
Displacement, L	0.552
Bore, mm	86.0
Stroke, mm	95.1
Connecting rod length, mm	166.7
Piston pin offset, mm	-1.55
Compression ratio	12:1
Operating condition	
Speed, rpm	1000
Intake temperature, °C	100
Coolant temperature, °C	90
Intake pressure, kPa	111
Exhaust pressure, kPa	100
Global equivalence ratio	0.5
Spark timing, °CA	-27
Early injections	
Timing, °CA	-318/-303/-288
Duration (each), μs	437
Fuel mass (all three), mg	20.34
Pilot injection	
Timing, °CA	-28
Duration, μs	210
Fuel mass, mg	0.84

is the turbulent diffusivity, κ is flame front curvature, and ρ_u is the unburned mixture density. The scalar $\tilde{G}$ indicates the distance from a local cell to the flame front ($\tilde{G}=0$). Variance of the mean or the filtered flame front is accounted for by the variance of G, $\widetilde{G''}$. Turbulent flame propagation speed S_T is modeled based on Peter's formula [25] in RANS,

$$S_T = S_L + u'\left(-\frac{a_4 b_3^2}{2b_1}Da + \left[\left(\frac{a_4 b_3^2}{2b_1}Da\right)^2 + a_4 b_3^2 Da\right]^{1/2}\right), \tag{2}$$

where u' is the root mean square of the turbulent fluctuating velocity, a_4, b_1, and b_3 are model constants, and Da is the Damköhler number defined as the ratio of a flame timescale to a turbulence timescale. In LES, Pitsch's formula [26] is employed,

$$S_T = S_L\left(1 - \frac{b_3^2 S_L \mu_T}{2b_1 \mu u'} + \sqrt{\left(\frac{b_3^2 S_L \mu_T}{2b_1 \mu u'}\right)^2 + \frac{b_3^2 \mu_T}{\mu}}\right), \tag{3}$$

where u' is the sub-grid scale velocity, and μ and μ_T are molecular and turbulent viscosities, respectively. Both formulas in Eqs. (2) and (3) involve the laminar flame speed S_L, which is calculated in this study using one-dimensional (1D) unstrained premixed laminar flames and tabulated as a function of local pressure (p), unburned temperature (T_0), equivalence ratio (ϕ), RGF (γ), in the ranges of 2 atm $< p <$ 60 atm, 300 K $< T_0 <$ 1200 K, $0.2 < \phi < 1$, $0 < \gamma < 0.1$, with intervals of 2 atm, 100 K, 0.1, and 0.05, respectively. In the hybrid model, except for the flame front which is tracked by Eq. (1), all other regions (including both burned and unburned mixtures) are solved using finite rate chemistry with the laminar closure. The laminar closure has been found sufficient in regions where local mesh is reasonably refined [24] and the gradients of most scalars are relatively low, e.g., in the regions far from the flame fronts in the current study. The use of finite rate chemistry is critical to capturing autoignition in the unburned mixture and the post flame (e.g., diffusion flame) in the burned region. Finite rate chemistry is further accelerated by the multi-zone approach [27]. The gas phase fuel surrogate is a blend of toluene primary reference fuel and ethanol based proposed in a previous study [15]. For both flame speed tabulation and finite rate chemistry modeling, a 164-species skeletal mechanism [15] is used to describe the chemical kinetics for the E30 fuel surrogate.

Non-uniform mesh with a base grid size of 4 mm is adopted. A fixed grid embedding of 0.25-0.5 mm is applied during spray injection and near the walls. A fine resolution of 0.125 mm is applied in a spherical region enclosing the spark gap for capturing early flame development. Adaptive mesh refinement with a minimum grid size of 0.5 mm is adopted to better resolve the

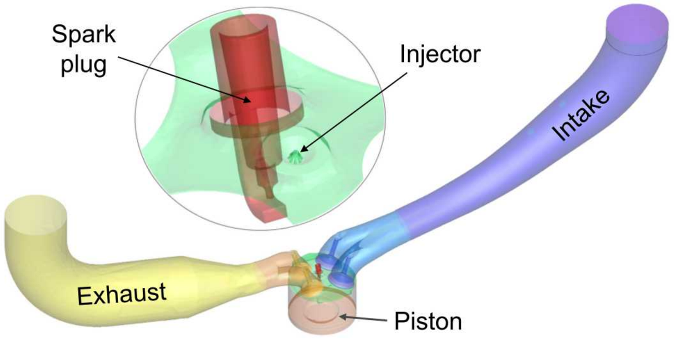

FIGURE 2: DISI engine geometry used in CFD.

flame and the velocity gradient. The resultant mesh consists of a peak cell count of approximately 1.6 million in LES and approximately 1.2 million in RANS.

3 RESULTS AND DISCUSSION

3.1 Spray Model Validation

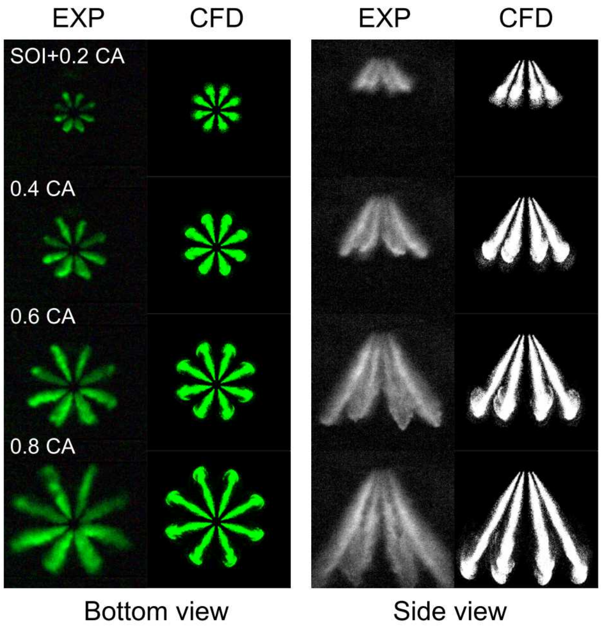

FIGURE 3: Spray patterns from the bottom and side views predicted from the RANS simulation compared with experiments for motored engine operation with pilot injection only. For these particular validation experiments, a lower intake temperature (30°C) and a longer injection duration of 325 μs was used to be consistent with Ref. [3], with an IR-camera setup that is described in Ref. [28].

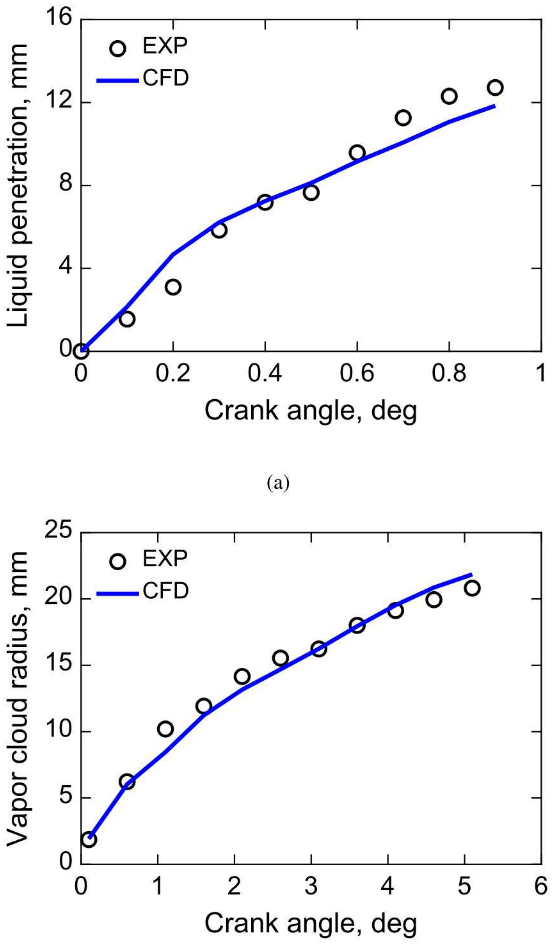

(a)

(b)

FIGURE 4: Evolution of (a) liquid penetration length and (b) the effective vapor cloud radius, for motored engine operation with pilot injection only.

For PFS engine operation, accurate descriptions of spray and vapor dynamics due to pilot injection are essential to establishing the proper mixture distribution near the spark plug gap. Due to the drastically different thermodynamic conditions, such as pressure and temperature, the spray topology (e.g., the cone angle and the included angle) may be different for the pilot injection compared with early injections. To this end, the bottom view and side view spray topologies measured in the experiment as shown in Fig. 3 are analyzed, based on which a cone angle of 25° and included angle 31.5° are identified. The experimentally-derived cone angle and included angle are then used in motored engine simulations for the pilot injection only operation, prior to performing multi-cycle fired engine simulations. Figure 3 compares spray patterns from the RANS simulation and the experiment from the bottom and side views for one engine cycle. Note that little cycle-to-cycle variation is observed for spray characteristics. As seen in Figure 3, very good agreement is observed between the RANS simulation and experiments. LES predicts similar liquid patterns and therefore is not shown. More quantitatively, experimental images are digitized to extract the borders of spray and vapor patterns. Liquid penetration length (L_{lp}) is then calculated based on the components obtained from both bottom view and side view,

$$L_{lp} = (\overline{L^r_{lp}}^2 + \overline{L^z_{lp}}^2)^{1/2}, \qquad (4)$$

where L^r_{lp} and L^z_{lp} indicate projections of L_{lp} in the bottom and side views, respectively. $\overline{L^r_{lp}}$ is the average over all eight spray plumes, while $\overline{L^z_{lp}}$ is the average over the four distinguishable

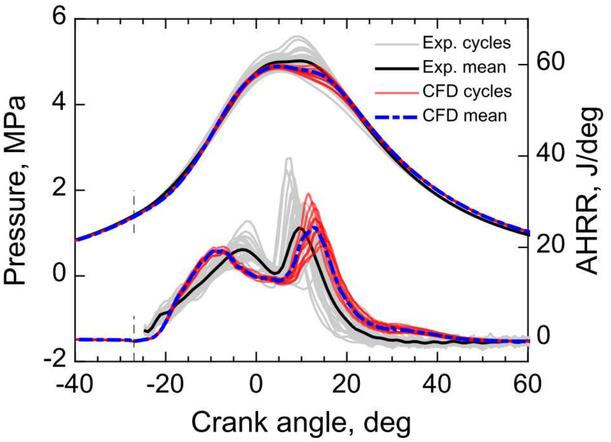

FIGURE 5: Predicted pressure and apparent heat release rate profiles from RANS compared with experiment. Individual experimental cycles and their mean values, and individual numerical cycles and their mean values are shown in gray, black, red, and blue lines, respectively.

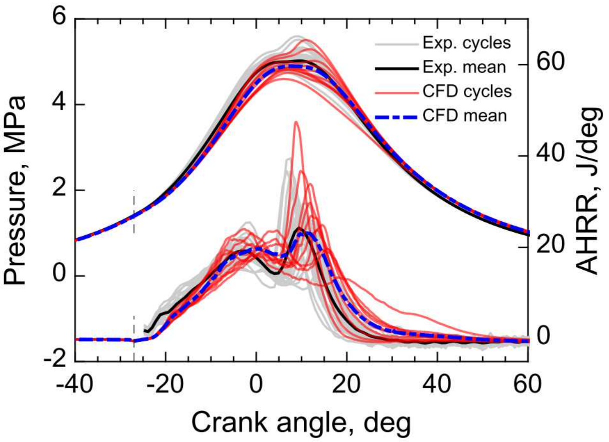

FIGURE 6: Predicted pressure and apparent heat release rate profiles from LES compared with experiment. Individual experimental cycles and their mean values, and individual numerical cycles and their mean values are shown in gray, black, red, and blue lines, respectively.

spray plumes, as seen in Fig. 3. For simulations, line-of-sight spray images are first constructed based on liquid volume fraction, and then the same procedure is performed to obtained the liquid penetration length. For vapor characterization, the effective vapor cloud radius (vapor plume length relative to the vapor cloud center from the bottom view) instead of the actual vapor penetration length is employed, as only the bottom view is available from the experiments. Similar to liquid penetration length, the effective vapor cloud radius is the averaged over 8 vapor plumes. Figure 4 compares numerical results of the liquid penetration length and the effective vapor cloud radius with experiments. Good agreement is achieved between simulations and experiments, suggesting that the current spray model setup is sufficiently accurate in capturing spray patterns and dynamics, as well as the subsequent evaporation process during and after the pilot injection.

3.2 Overall Performance of the CFD Model

Using the realistic spray cone angle and included angle in Lagrangian spray models, the CFD model is then applied to simulate fired engine operation, and is validated against experimental data. Figures 5 and 6 show the predicted pressure and apparent heat release rate (AHRR) traces from ten consecutive simulation cycles from RANS and LES respectively, compared with 32 skip-fired experimental cycles. Here, the ten simulation cycles are used to obtain statistically meaningful ensemble average of pressure and AHRR profiles. Results from the RANS simulation show a reasonable agreement with experiments in terms of the mean pressure and AHRR traces. Both combustion modes, namely early deflagration and late autoignition, are reasonably captured in RANS, while visible discrepancies are observed in the locations for peak pressures and peak AHRRs corresponding to both combustion modes. In addition, negligible level of CCV for deflagration, and moderate CCV for autoignition, are predicted by RANS, which is expected since RANS based models, by design, are intended to capture the mean rather than the fluctuations of a given quantity. In contrast, as seen in Fig. 6, LES significantly improves the prediction of mean and CCV for both the pressure and the AHRR traces, especially the prediction of combustion phasing. Moreover, larger CCV is observed for the peak pressure and peak AHRR associated with autoignition (second peak) than those associated with deflagration (first peak). This can be explained as follows. First, the temperature of the end-gas is directly affected by the combustion phasing of the deflagration-based combustion. Second, in addition to temperature, the autoignition process is also sensitive to radicals in

TABLE 2: Predicted and measured mean combustion characteristics.

Quantity	Experiment	RANS	LES
P_{max}, bar	50.6	48.9	49.5
P'_{max}, bar	2.0	0.29	2.6
IMEP$_n$, bar	5.75	6.17	6.18
CoV, %	1.29	0.58	1.48
CA10, °CA	-14.2	-13.5	-11.2
CA50, °CA	1.83	3.2	4.3
CA90, °CA	16.7	19.0	18.6

the end-gas that can be either from the residual gas or from the partially-reacted fresh mixture. Such temperature and radical dependences along with the CCV of the flow field result in larger cyclic variability of the second peak AHRR.

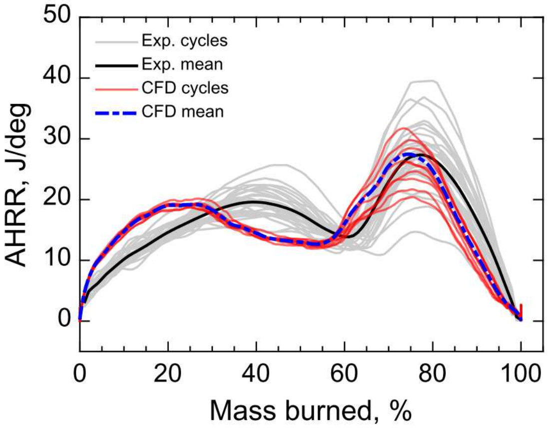

(a) RANS

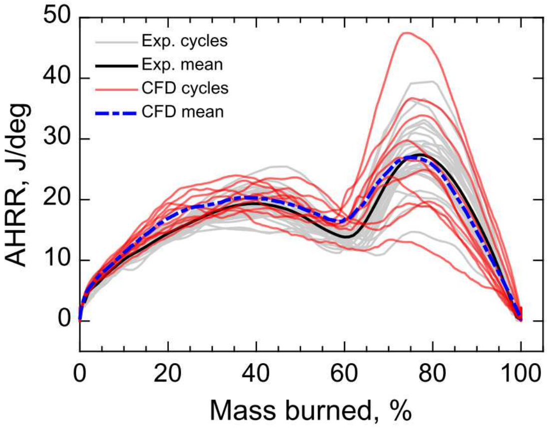

(b) LES

FIGURE 7: Predicted apparent heat release rate in the burned mass fraction space from (a) RANS and (b) LES, respectively, compared with experiment.

Table 2 quantitatively compares several key engine performance metrics calculated from simulations and experiments, including mean and standard deviation of the peak cylinder pressure (P_{max}), mean and coefficient of variation (CoV) of the net indicated mean effective pressure (IMEP_n), and combustion phasing corresponding to 10% (CA10), 50% (CA50), and 90% (CA90) of the total heat release. Both RANS and LES show good agreement with the experiment in the mean peak pressure with relative errors of 2% and 3%, respectively. IMEP_n is slightly over-predicted (by 7%) using both RANS and LES, which can be attributed to the uncertainty in the thermal wall boundary condition given that detailed wall temperature measurement is not available in the experiment. Such discrepancy may also be attributed to insufficient description of flame-wall interaction in the current G-equation model, which merits further investigation. Both RANS and LES simulations show a consistently larger CA10 and CA50 than the experiment, and is consistent with the slight delay in SoC observed in Figs. 5 and 6. This may be due to the slight under-prediction of liquid evaporation, which will be further detailed in Section 3.3. Clearly, LES shows a large advantage over RANS on capturing the cyclic variations in the peak pressure and IMEP_n.

The improved model accuracy of the LES-based model is further demonstrated in Fig. 7, where the AHRR profiles are plotted in the burned mass fraction (ξ) space. The burned mass fraction is calculated based on the accumulative AHRR normalized by its peak value at the end of combustion (EoC). The experimental AHRR peaks at $\xi = 0.39$ and 0.77 respectively, signifying the deflagration and autoignition modes, with its transition occurring at $\xi = 0.6$. The LES-based model accurately captures the phasing associated with the two modes ($\xi = 0.375$ and 0.745, respectively) and the transition point ($\xi = 0.59$). However, the RANS-based model fails to capture the phasing of peak AHRRs, especially for the deflagration mode, resulting in an error of 33% compared with a 4% error using LES. The observed model deficiency of RANS suggests the need of further improvement of the G-equation model in the RANS context, e.g., to better account for the strain effect on flame propagation that has been conventionally neglected [25].

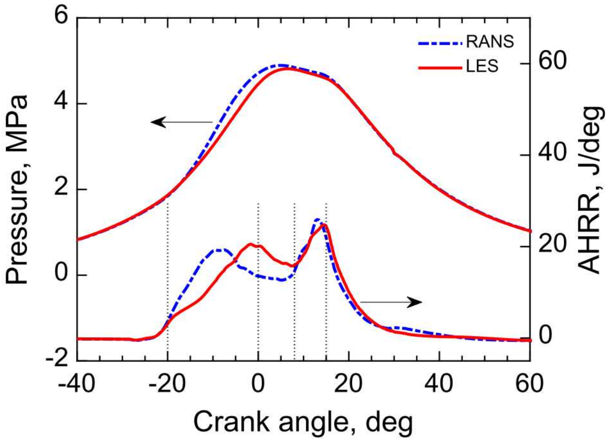

FIGURE 8: Pressure and AHRR profiles for two selected cycles from RANS and LES, respectively. The vertical dotted lines indicates -20, 0, 8, and 15 °CA, respectively.

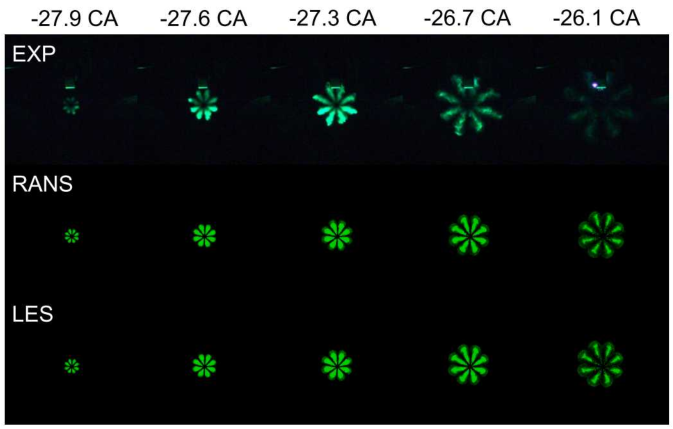

FIGURE 9: Liquid spray morphology at different time snapshots, comparing experimental Mie-scattering light intensity with numerical predictions of line-of-sight liquid volume fraction using RANS and LES, respectively.

3.3 Spray and Flame Structures

Individual in-cylinder processes in PFS-assisted SACI combustion, including pilot spray injection, mixing, flame propagation, and end-gas autoignition are further analyzed in detail based on 3D simulations data. Representative experimental and simulation cycles are selected such that they have a comparable peak AHRR with the ensemble mean from the experiment. The pressure and AHRR profiles for the two selected simulation cycles from RANS and LES respectively are shown in Fig. 8.

Figure 9 shows the spray patterns for the two cycles in Fig. 8 that are predicted by RANS and LES models, respectively. Spray patterns from optical imaging enabled by LED illumination are also compared. Both RANS and LES predict quite similar spray structure and penetration length, indicating the negligible impact of the flow field on spray characteristics, due to its large injection momentum. Both RANS and LES simulations show limited spray-to-spray interactions, which are similar to the experimental observations. The diminished experimental spray signal at -26.1 CA, probably indicating strong evaporation, is also captured in simulations, although a small shift in the crank angle space was observed. Both RANS and LES simulations, however, show a smaller spray penetration length than the experiment. This can be probably explained by the differences in injection duration (210 vs. 325 μs) and intake temperature (100 vs. 30 °C) between the fired and motored cases (Section 3.1). The

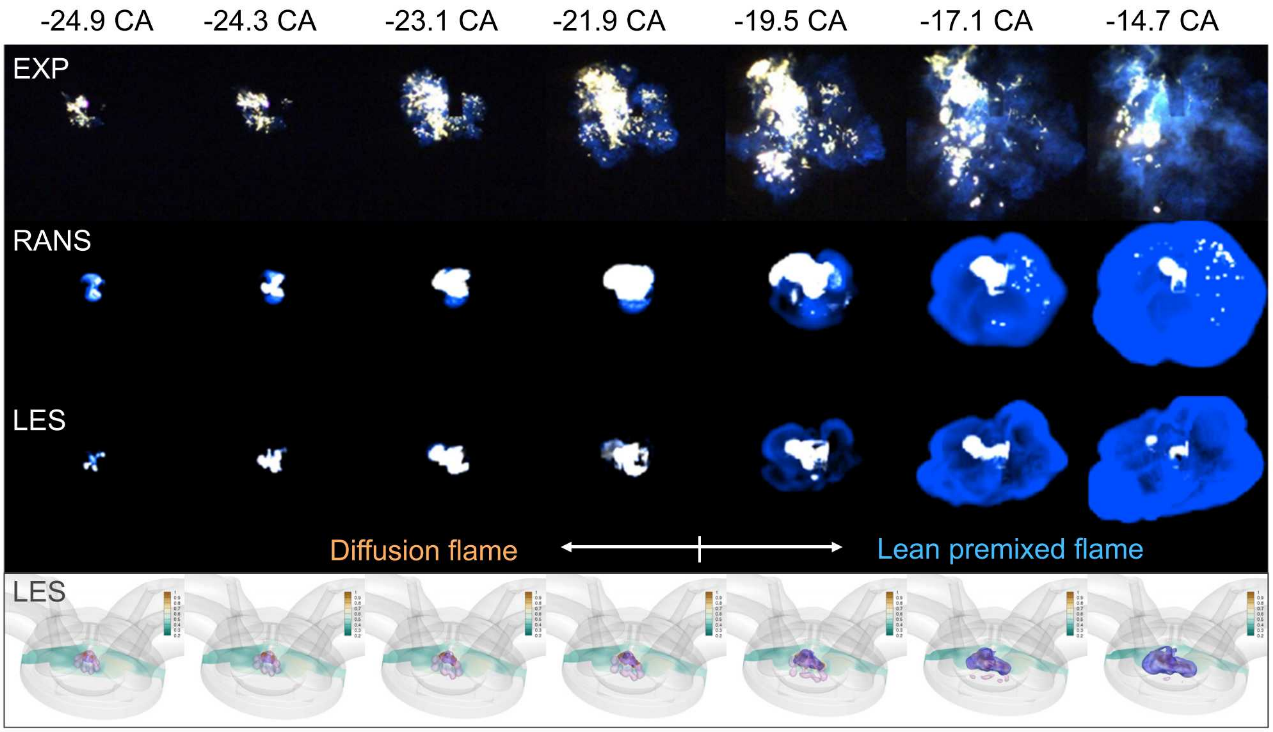

FIGURE 10: First three rows: Flame structure observed in the experiment and in simulations using RANS and LES. respectively. For both simulations, bright color is synthesized with C_2H_2 concentration, while the blue color is synthesized with the product of OH and CH_2O concentrations. Last row: Evolution of the stoichiometric iso-surface (purple) and deflagration flame fronts (blue) along with equivalence ratio contours on a $x-z$ cross-section cutting through the center of the spark gap.

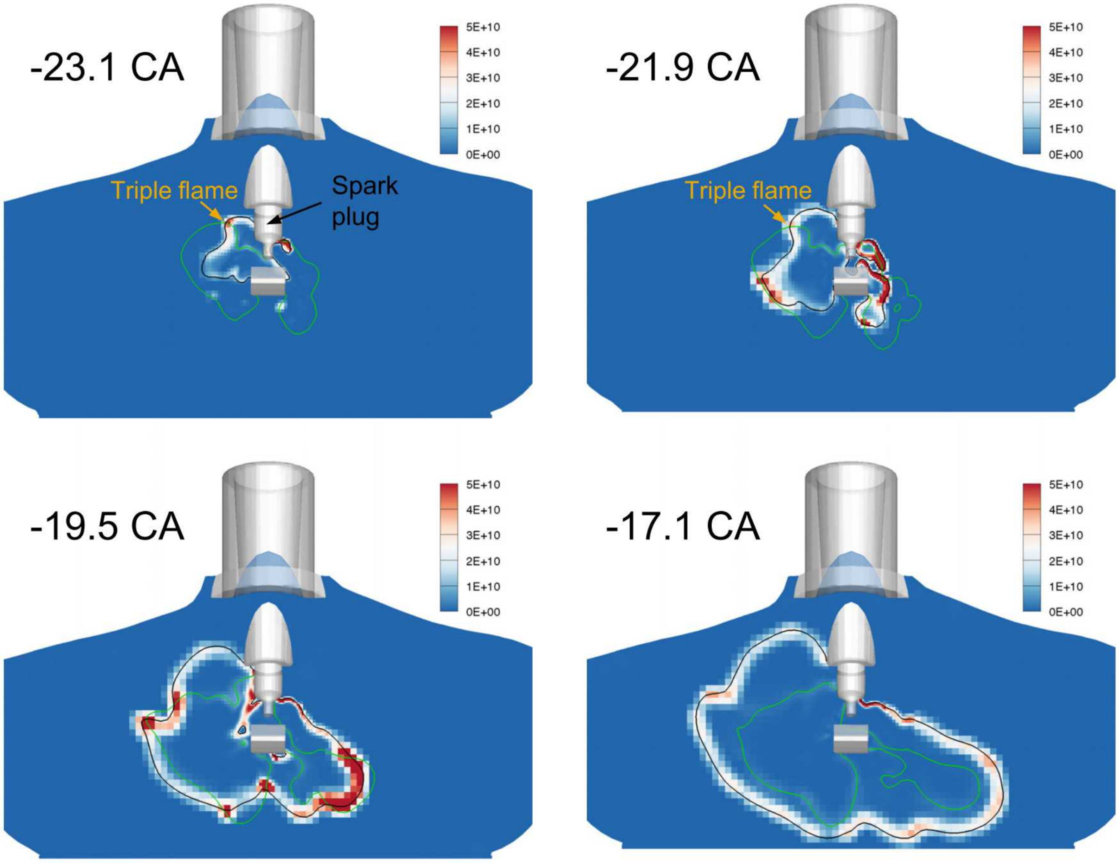

FIGURE 11: Distribution of local heat release rate (J/m^3·s) on a cross-section cutting through the spark plug gap in LES. Black isoline indicates the premixed flame front ($\tilde{G} = 0$). Green isoline indicates the stoichiometric mixture ($\phi = 1$).

pilot-injection rate of injection (ROI) profile (which works well for the motored simulations) may not be consistent with that in experiments for the fired case due to the increasingly more relevant opening and closing transients with shorter pilot injection. This is a common limitation of the Lagrangian spray models in predicting highly transient near-nozzle behaviors. Further improvement is possible by incorporating more detailed information of ROI from experiments or through one-way coupling with internal nozzle flows. This, however, requires further investigation. Moreover, the under-prediction of liquid penetration is probably the cause of the delay in SoC (Figs. 5 and 6) because a smaller liquid penetration can delay the spray-driven spread of the flame from the spark plug gap into the combustion chamber.

Flame dynamics of two representative cycles in Fig. 8 predicted from RANS and LES simulations are compared with measured flame structure based on natural luminescence in Fig. 10. Bright color in the experiment represents the high-sooting diffusion flame or rich premixed flame, while the blue color indicates the lean premixed flame. To enable comparison between simulations and experiments, false color images are constructed from line-of-sight projection of 3D simulation data. In particular, since soot is not modeled in the current study, the bright color is mimicked by C_2H_2 which is a widely used soot precursor (e.g., in the two-equation soot model [29]). The blue color is typically due to emission of highly energetic radicals such as CH* which is only present at the flame fronts. Since CH* is not readily available from the current chemical mechanism, $[OH]\times[CH_2O]$ ([] denotes the molar concentration), a premixed flame indicator that is commonly used experimental diagnostics [30], is used to indicate the lean premixed flames. The transition from a sooting flame to a non-sooting lean premixed flame is well captured by both RANS and LES models. From instantaneous flame typology point of view, RANS simulation shows a near-spherical flame development, while LES predicts more winkles in the flame fronts which exhibit a preferential orientation similar to the experimental measurement at -19.5 °CA. This preferential orientation is probably determined by the local flow condition, and is not observed in the simulation. Corresponding 3D flame structure are also shown in the last row. Deflagration flame fronts are shown in blue ($\tilde{G} = 0$), and the sto-

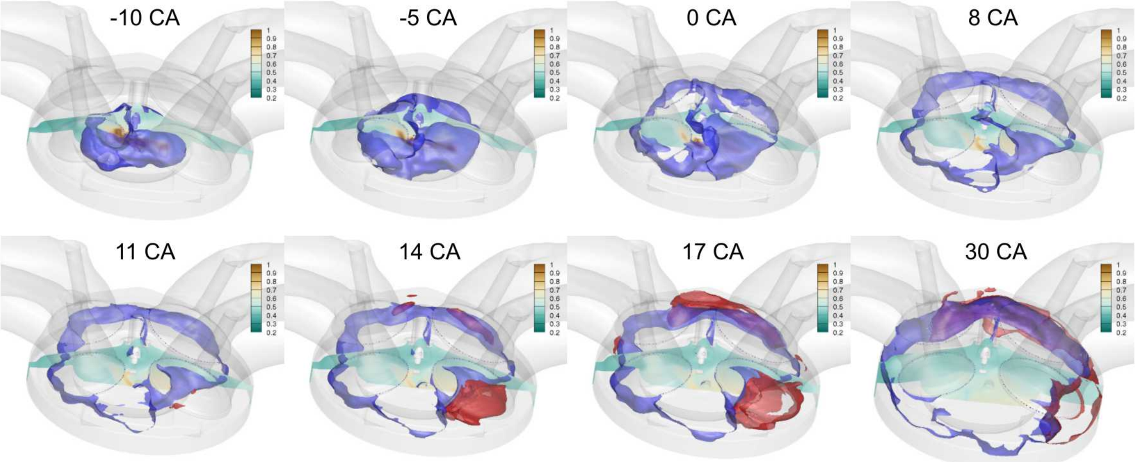

FIGURE 12: Evolution of the stoichiometric iso-surface (purple), deflagration flame fronts (blue), and autoignition pockets (red), in a representative LES cycle. The contours indicate equivalence ratio profiles on a $x-z$ cross-section cutting through the center of the spark gap.

ichiometric isosurface is shown in purple. The equivalence ratio distribution is shown on a 2D plane cutting through the spark plug gap. Clearly, as early combustion transitions from sooting to non-sooting flames, rich mixtures are quickly consumed, and flames propagate into lean mixtures.

To further depict the combustion modes associated with the early-stage sooting flame, Fig. 11 shows the contour of local heat release rate on a 2D plane cutting through the spark plug gap for the LES cycle. Isolines of $\tilde{G}=0$ and $\phi=1$ are superimposed to delineate the local flame structure. It is clear that early-stage flames (-17.1 and -21.9 °CA) are a combination of lean and rich premixed flames along with a stoichiometric diffusion flame that forms a canonical “triple flame” structure. As rich mixtures are consumed by the premixed flame front (-17.1 °CA), the whole $\phi=1$ isoline is enclosed by the $\tilde{G}=0$ isoline, indicating fresh mixtures start to burn purely in the lean premixed flame mode. It is worth noting that successful prediction of such transition is enabled by the combined usage of G-equation for flame propagation and finite rate chemistry in the post-flame zone.

As flame propagates toward the cylinder wall, the unburned fresh mixture between the flame and the wall is commonly referred to as ”end-gas” (identified by $\tilde{G}<0$ when the G-equation model is used), which has the potential to auto-ignite when the temperature and pressure become sufficiently high. Figure 12 shows the stoichiometric isosurfaces (purple), deflagration flame fronts (blue), the autoignition pockets (red) and the cross-sectional equivalence ratio distribution for the same LES cycle. Here, the deflagration flame fronts are identified by $\tilde{G}=0$, while the autoignition pockets are identified by large concentration of the major combustion product H_2O, i.e., $Y_{H_2O}/Y_{H_2O}{}^{eq}=70\%$ in the region where $\tilde{G}<0$. It is clearly seen that the pilot injection creates a locally stratified mixture ranging from rich to lean conditions. This stratified mixture lasts for approximately 10 crank angles until either quickly consumed by flame or diluted by the lean background mixture. The presence of locally near-stoichiometric mixture provides a stable mechanism for initial flame propagation with larger flame speed, thus stabilizing the overall combustion process. As the stratified fresh mixture is completely consumed, the flame continues to propagate in the lean background until autoignition takes place in the end-gas when the in-cylinder temperature and pressure become sufficiently high. The autoignition event evolves in a much shorter duration than deflagration and thus avoids retarded combustion phasing.

The nature of sequential autoignition in the end-gas is similar to that in homogeneous charge compression ignition (HCCI), the intensity of which is closely related to the available stratification levels of temperature and equivalence ratio [5, 31]. It is therefore worthwhile to investigate temperature and mixture distributions in the end-gas to understand the knock mitigation mechanisms. Figure 13 shows the probability density functions (PDF) of the temperature and the normalized equivalence ratio ($\phi_n=\phi/(\phi+1)$) in the end-gas at various crank angles, ranging from spark timing, to transition of flame mode, and to the timing just prior to autoignition. Here, ϕ_n instead of ϕ is used so that contributions from extremely rich mixtures can be more conveniently quantified and visualized in the ϕ_n space. As time evolves, the mean temperature monotonically increases due to the compression of the end-gas by piston motion and flame propagation. The stratification level in temperature also increases due to continuous heat loss to the wall. The mean end-gas equivalence ratio remains largely unchanged, while the stratification level first increases due to spray evaporation (from -27 to -22 °CA), and then decreases due to the consumption of the

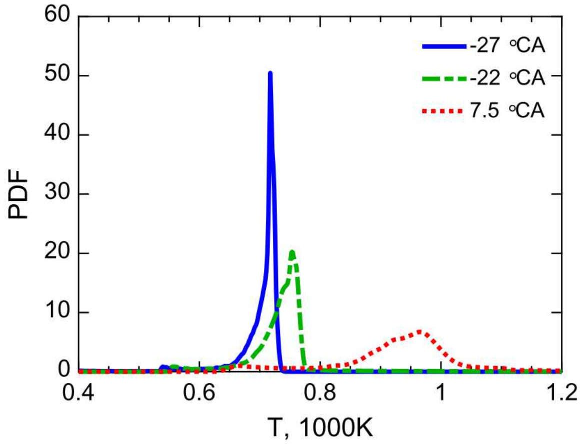

(a) Temperature stratification

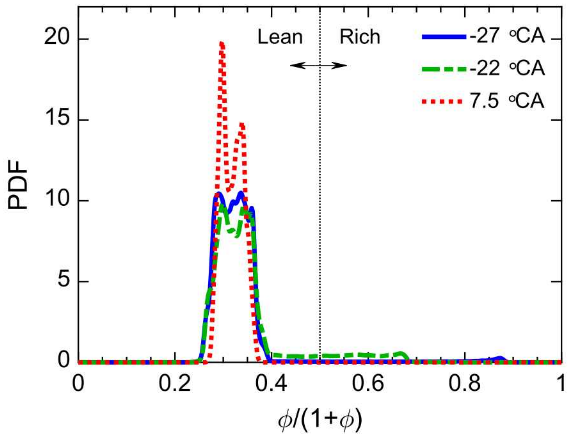

(b) Equivalence ratio stratification

FIGURE 13: PDF of (a) temperature and (b) normalized equivalence ratio ($\phi/(\phi+1)$)) in the end-gas at different crank angles corresponding to the spark timing (-27 °CA), the transition from a sooting flame to a non-sooting premixed flame (-22 °CA), and the transition from deflagration to autoignition (7.5 °CA). The vertical line indicates stoichiometry.

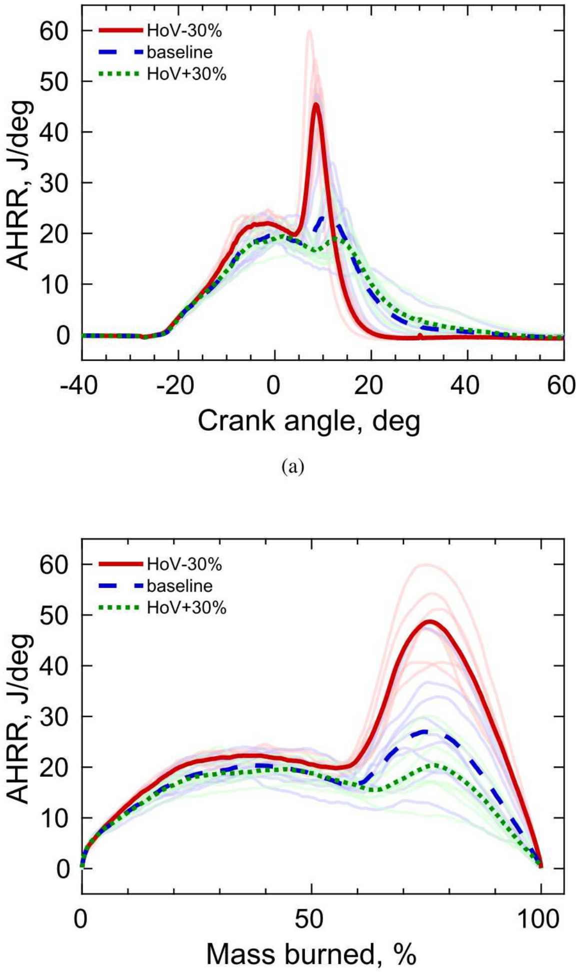

(a)

(b)

FIGURE 14: AHRR traces in (a) the crank angle coordinate and (b) the burned mass fraction coordinate for PFS operation, in response to perturbations of HoV. Light thin lines represent individual cycles while dark thick lines indicate their mean.

stratified fuel and the persistent mixing process. The presence of non-negligible stratification in temperature and equivalence ratio may play an important role in mitigating excessive engine knock for the SACI operation, which will be a topic for future investigation.

3.4 Fuel Properties Effects: HoV & Flame Speed

With the demonstrated capability on capturing the in-cylinder mixing and combustion processes in PFS-assisted SACI, the CFD model is employed to systematically investigate impacts of fuel properties. Different from previous studies [10, 32] which used the lower-fidelity RANS model, the higher-fidelity LES model is employed for the sensitivity analysis. In particular, heat of vaporization (HoV) and laminar flame speed (S_L) are of interest, and perturbations are applied to baseline HoV and S_L values with a fixed spark timing (-27 °CA). Here, the laminar flame speed is assumed as a fuel property that is independent of the autoignition propensity for a given fuel. Therefore, when perturbation is applied to S_L, the chemical kinetic parameters for the finite rate chemistry modeling remain unchanged. While an alternative way to perform sensitivity analysis is to perturb the chemical kinetic parameters for both flame speed calculation and finite rate chemistry modeling, the method used in the current study allows isolated investigation of individual fuel properties (which is nevertheless challenging in experiments), thus providing physical insights to the search of new fuels that might bring engine efficiency benefits with tailor-made fuel properties. For each perturbation, ten consecutive cycles are simulated to achieve statistically steady state.

Figure 14 shows the AHRR traces in both the crank angle space and in the mass burned space, for HoV perturbed by ±30% relative to its baseline value. A decrease in HoV is seen to slightly advance deflagration combustion phasing while significantly accelerating autoignition and advancing the phasing. Interestingly, although the peak autoignition AHRR drops dramatically, the combustion phasing in the mass burned space remains unaffected for both deflagration and autoignition. The observed HoV sensitivity is mainly due to the charge cooling effect in the cylinder especially for direct injection engines, where a lower HoV normally leads to a higher fresh mixture temperature and thus higher flame speed and shorter ignition delay time. This is confirmed by Fig. 15 where CA50 and intake valve closing (IVC) temperature for the PFS operation are plotted as functions of the HoV perturbation and compared with those for the well-mixed operation reported in a previous study [15]. Similar sensitivities of CA50 and IVC temperature are observed for both PFS and well-mixed operations, except that the well-mixed operation exhibits a non-monotonic trend in CA50 due to the excessive level of CCV.

Figure 16 shows the pressure traces, and the AHRR traces in both the crank angle coordinate and the mass burned space, for S_L perturbed by ±10%, ±30%, and ±50% relative to its baseline value, respectively. The relatively large perturbations of ±50% are included to mimic the fuels with extremely low (e.g., ammonia) and high (e.g., hydrogen) flame speeds, respectively. The

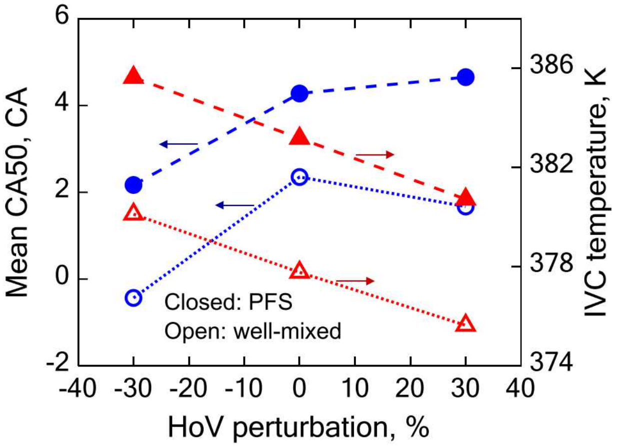

FIGURE 15: HoV sensitivities of CA50 and in-cylinder temperature at IVC, comparing SACI operation with well-mixed charge (Ref. [15]) and with PFS (this study).

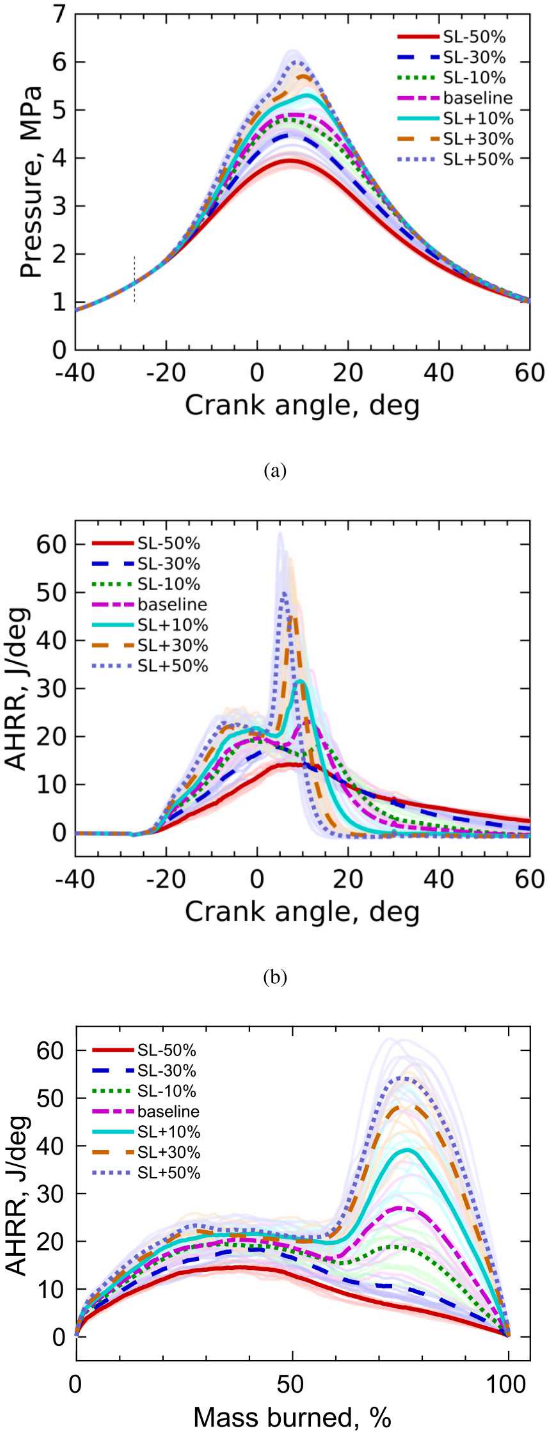

(a)

(b)

(c)

FIGURE 16: (a) Pressure traces, (b) AHRR traces in the crank angle coordinate and (c) in the burned mass fraction coordinate for PFS operation, in response to perturbations of S_L. Light thin lines represent individual cycles while dark thick lines indicate their mean.

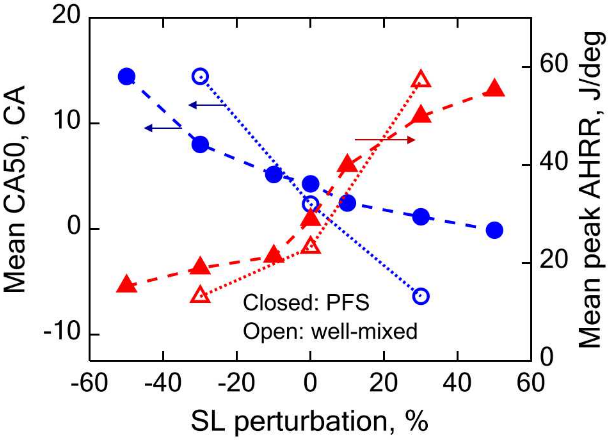

FIGURE 17: S_L sensitivities of CA50 and IVC temperature, comparing SACI operation with well-mixed charge (Ref. [15]) and with PFS (this study).

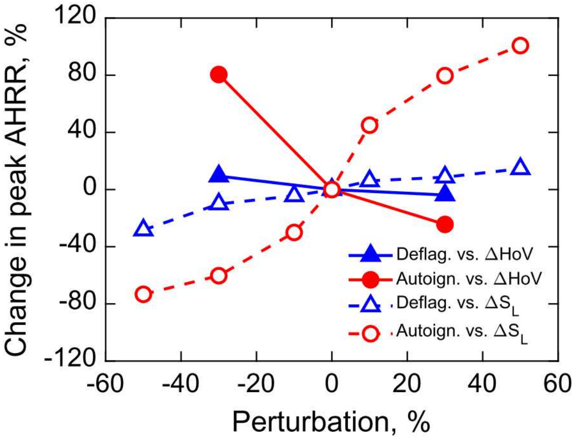

FIGURE 18: Changes in peak AHRRs due to deflagration and autoignition, respectively, in response to HoV and S_L perturbations for PFS operation.

value of S_L is found directly associated with the initial ramp-up rates and the peak values of both pressure and AHRR during deflagration in the crank angle coordinate. The enhanced deflagration by a larger S_L further promotes autoignition by raising pressure and temperature in the end-gas, thus simultaneously advancing the combustion phasing and increasing the peak pressure and AHRR during autoignition in the crank angle coordinate. Similar to HoV, the change in S_L does not modify the combustion phasing in the mass burned space. In Fig. 17, the S_L sensitivities of CA50 and peak AHRR for the PFS operation are further compared with those for the well-mixed charge operation described in Ref. [15]. Despite the similar trends of increasing peak AHRR and advanced CA50 against S_L, the PFS operation shows a smaller sensitivity to S_L compared with the well-mixed operation, which can be attributed to the improved combustion phasing control capability of PFS. For lean well-mixed operation, there is a relatively long induction period from the spark until the main combustion event, making the combustion phasing very sensitive to changes of the flame speed. For PFS operation, Fig. 17 reveals a change in the slopes of CA50 and peak AHRR at the perturbation of -10% as S_L increases, coinciding with the transition in the dominant combustion mode, i.e., from the deflagration-only mode to the mixed deflagration-autoignition mode (evident in Fig. 16c).

The sensitivities of the two peak AHRRs (associated with deflagration and autoignition, respectively) to HoV and S_L are further quantified in Fig. 18. Clearly, the autoignition peak AHRR shows a non-linear response to S_L, in contrast to the near-linear response of the deflagration peak AHRR. In addition, the peak AHRR due to autoignition is much more sensitive to either HoV or S_L than that due to deflagration. Therefore, to avoid excessive combustion noise and engine knock, controlling the autoignition-based peak AHRR is the primary concern when fuels of different laminar flame speeds are used. In a practical implementation, this can be achieved by adjusting the spark timing, preferably via closed-loop feedback using a cylinder pressure sensor.

4 CONCLUSIONS

A multi-cycle LES-based CFD model was developed in this study for lean SACI combustion assisted by the PFS fueling strategy in a DISI engine. Spray model setup was first improved to accurately represent the spray morphology during pilot injection. The modified spray model setup showed good agreement in liquid and vapor penetrations with experimental measurements. PFS-assisted SACI combustion was modeled by a hybrid combustion model coupling level-set G-equation model and well-stirred reactor model for flame propagation and end-gas autoignition. Good agreement was observed between multi-cycle LES simulations and experimental data, in terms of mean and variations in pressure and heat release rate traces. LES also well predicted mean and fluctuations of global quantities such as peak pressure, IMEP, and combustion phasing. In comparison, multi-cycle RANS simulations failed to capture CCV and showed larger deviations in the combustion phasing, especially the location of peak heat release due to deflagration, while it captured the mean pressure and IMEP reasonably well. Pilot injection, combustion, and mixing processes were analyzed in detail. LES and RANS showed similar predictions in spray dynamics. LES captured flame wrinkling and a preferential flame orientation similar to experimental observations. In contrast, RANS predicted a smoother, spherical flame topology. With LES, the canonical triple flame structure was identified at the early stage of flame propagation before transitioning into lean-premixed flames. Non-negligible stratification in the end-gas was observed for both temperature and equivalence ratio, which may play an important role in smoothing out the peak heat release rate during sequential autoignition.

The LES-based CFD model was then leveraged to investigate fuel property effects by perturbing the HoV and S_L of the fuel. HoV was found to play an important role by modifying the unburned gas temperature and thus combustion phasing, and its sensitivity for the PFS operation is comparable with that for the well-mixed charge operation. A perturbation of S_L is found to directly modify the initial ramp-up rate and peak values of the deflagration AHRR and subsequently affect end-gas autoignition through changes in temperature and pressure. Compared with the well-mixed charge operation, PFS operation shows a smaller S_L sensitivity. It is found that either a smaller HoV or a larger S_L would advance CA50 and increase the peak AHRR, and the sensitivity of autoignition peak AHRR is much larger than that of deflagration peak AHRR. The identified fuel property sensitivities through local perturbations shed light on future research of quantifying fuel property effects on knock limit and on optimal engine efficiency toward co-optimization of fuels and PFS-assisted lean SACI engine operation.

ACKNOWLEDGMENT

UChicago Argonne, LLC, operator of Argonne National Laboratory ("Argonne"), a U.S. Department of Energy (DOE) Office of Science laboratory, is operated under Contract No. DE-AC02- 06CH11357. The U.S. Government retains for itself, and others acting on its behalf, a paid-up nonexclusive, irrevocable worldwide license in said article to reproduce, prepare derivative works, distribute copies to the public, and perform publicly and display publicly, by or on behalf of the Government. This research was partially funded by DOE's Office of Vehicle Technologies, Office of Energy Efficiency and Renewable Energy under Contract No. DE-AC02-06CH11357. The authors wish to thank Gurpreet Singh, Michael Weismiller, and Kevin Stork, program managers at DOE, for their support. This research was conducted as part of the Co-Optimization of Fuels & Engines (Co-Optima) project sponsored by the U.S. DOE's Office of Energy Efficiency and Renewable Energy (EERE), Bioenergy Technologies and Vehicle Technologies Offices. We gratefully acknowledge the computing resources provided on Bebop, a high-performance computing cluster operated by the Laboratory Computing Resource Center at Argonne National Laboratory. The engine experiments were performed at the Combustion Research Facility, Sandia National Laboratories, Livermore, CA. Cinzia Tornatore of Istituto Motori is acknowledged for contributions to the spray and flame imaging presented in this study. Sandia National Laboratories is a multi-mission laboratory managed and operated by National Technology and Engineering Solutions of Sandia, LLC., a wholly owned subsidiary of Honeywell International, Inc., for the U.S. Department of Energy's National Nuclear Security Administration under contract DE-NA0003525.

REFERENCES

[1] "World Energy Outlook 2019". IEA (2019), IEA, Paris, https://www.iea.org/reports/world-energy-outlook-2019.

[2] Arcoumanis, C., and Kamimoto, T., 2009. *Flow and combustion in reciprocating engines*. Springer Science & Business Media.

[3] Hu, Z., Zhang, J., Sjöberg, M., and Zeng, W., 2019. "The use of partial fuel stratification to enable stable ultra-lean deflagration-based Spark-Ignition engine operation with controlled end-gas autoignition of gasoline and E85". *International Journal of Engine Research*. doi:`10.1177/1468087419889702`.

[4] Nakai, E., Goto, T., Ezumi, K., Tsumura, Y., Endou, K., Kanda, Y., Urushihara, T., Sueoka, M., and Hitomi, M., 2019. "Mazda Skyactiv-X 2.0 L Gasoline Engine". Proceedings of the 28th Aachen Colloquium Automobile and Engine Technology.

[5] Sjöberg, M., Dec, J. E., and Cernansky, N. P., 2005. "Potential of thermal stratification and combustion retard for reducing pressure-rise rates in HCCI engines, based on multi-zone modeling and experiments". *SAE Technical Paper 2005-01-0113 and SAE 2005 Transactions Journal of Engines-V114-3*. doi:`10.4271/2005-01-0113`.

[6] Yang, Y., Dec, J. E., Dronniou, N., and Sjöberg, M., 2011. "Tailoring HCCI heat-release rates with partial fuel stratification: Comparison of two-stage and single-stage-ignition fuels". *Proceedings of the Combustion Institute,* **33**(2), pp. 3047–3055.

[7] Szybist, J. P., and Splitter, D. A., 2017. "Pressure and temperature effects on fuels with varying octane sensitivity at high load in SI engines". *Combustion and Flame,* **177**, pp. 49–66.

[8] Kasseris, E., and Heywood, J., 2012. "Charge cooling effects on knock limits in SI DI engines using gasoline/ethanol blends: Part 2-effective octane numbers". *SAE International Journal of Fuels and Lubricants,* **5**(2), pp. 844–854.

[9] Kolodziej, C. P., Pamminger, M., Sevik, J., Wallner, T., Wagnon, S. W., and Pitz, W. J., 2017. "Effects of fuel laminar flame speed compared to engine tumble ratio, ignition energy, and injection strategy on lean and EGR dilute spark ignition combustion". *SAE International Journal of Fuels and Lubricants,* **10**(1), pp. 82–94.

[10] Yue, Z., and Som, S., 2019. "Fuel property effects on knock propensity and thermal efficiency in a direct-injection spark-ignition engine". *Applied Energy*. doi:`10.1016/j.apenergy.2019.114221`.

[11] Miles, P., 2018. "Efficiency Merit Function for Spark-ignition Engines: Revision and Improvements

Based on FY16-17 Research". Technical Report. U.S. Department of Energy, Washington, DC. 2018. DOE/GO-102018-5041.

[12] Dahms, R., Felsch, C., Röhl, O., and Peters, N., 2011. "Detailed chemistry flamelet modeling of mixed-mode combustion in spark-assisted HCCI engines". *Proceedings of the Combustion Institute,* **33**(2), pp. 3023–3030.

[13] Middleton, R. J., Olesky, L. K. M., Lavoie, G. A., Wooldridge, M. S., Assanis, D. N., and Martz, J. B., 2015. "The effect of spark timing and negative valve overlap on spark assisted compression ignition combustion heat release rate". *Proceedings of the Combustion Institute,* **35**(3), pp. 3117–3124.

[14] Wang, X., Xie, H., Xie, L., Zhang, L., Li, L., Chen, T., and Zhao, H., 2013. "Numerical simulation and validation of SI-CAI hybrid combustion in a CAI/HCCI gasoline engine". *Combustion Theory and Modelling,* **17**(1), pp. 142–166.

[15] Xu, C., Pal, P., Ren, X., Som, S., Sjöberg, M., Van Dam, N., Wu, Y., Lu, T., and McNenly, M., 2019. "Numerical investigation of fuel property effects on mixed-mode combustion in a spark-ignition engine". Proceedings of the ASME 2019 Internal Combustion Engine Division Fall Technical Conference, Chicago, IL, October 20–23, 2019, V001T06A010, ASME. doi:`10.1115/ICEF2019-7265`.

[16] Joelsson, T., Yu, R., and Bai, X.-S., 2012. "Large eddy simulation of turbulent combustion in a spark-assisted homogeneous charge compression ignition engine". *Combustion Science and Technology,* **184**(7-8), pp. 1051–1065.

[17] Wang, X., and Zhao, H., 2017. "Multi-cycle large eddy simulation (LES) of the cycle-to-cycle variation (CCV) of spark ignition (SI) - controlled auto-ignition (CAI) hybrid combustion in a gasoline engine". *SAE Technical Paper 2017-01-2261*. doi:`10.4271/2017-01-2261`.

[18] Richards, K. J., Senecal, P. K., and Pomraning, E., 2018. "CONVERGE Manual (Version 2.4)". Convergent Science Inc., Madison, WI-USA.

[19] Reitz, R. D., 1987. "Modeling atomization processes in high-pressure vaporizing sprays". *Atomisation and Spray Technology,* **3**(4), pp. 309–337.

[20] Froessling, N., 1958. "Evaporation, heat transfer, and velocity distribution in two-dimensional and rotationally symmetrical laminar boundary-layer flow". Report No. NACA-TM-1432.

[21] Liu, A. B., Mather, D., and Reitz, R. D., 1993. "Modeling the effects of drop drag and breakup on fuel sprays". *SAE Technical Paper 930072 and SAE 1993 Transactions Journal of Engines-V102-3*. doi:`10.4271/930072`.

[22] Amsden, A. A., and Findley, M., 1997. "KIVA-3V: A block-structured KIVA program for engines with vertical or canted valves". Lawrence Livermore National Laboratory, Livermore, CA, USA.

[23] Pomraning, E., and Rutland, C. J., 2002. "Dynamic one-equation nonviscosity large-eddy simulation model". *AIAA Journal,* **40**(4), pp. 689–701.

[24] Pal, P., Kolodziej, C. P., Choi, S., Som, S., Broatch, A., Gomez-Soriano, J., Wu, Y., Lu, T., and See, Y. C., 2018. "Development of a virtual cfr engine model for knocking combustion analysis". *SAE International Journal of Engines,* **11**(2018-01-0187), pp. 1069–1082.

[25] Peters, N., 2000. *Turbulent Combustion*. Cambridge University Press, Cambridge.

[26] Pitsch, H., and De Lageneste, L. D., 2002. "Large-eddy simulation of premixed turbulent combustion using a level-set approach". *Proceedings of the Combustion Institute,* **29**(2), pp. 2001–2008.

[27] Babajimopoulos, A., Assanis, D., Flowers, D., Aceves, S., and Hessel, R., 2005. "A fully coupled computational fluid dynamics and multi-zone model with detailed chemical kinetics for the simulation of premixed charge compression ignition engines". *International Journal of Engine Research,* **6**(5), pp. 497–512.

[28] Zeng, W., Sjöberg, M., Reuss, D. L., and Hu, Z., 2017. "High-speed PIV, spray, combustion luminosity, and infrared fuel-vapor imaging for probing tumble-flow-induced asymmetry of gasoline distribution in a spray-guided stratified-charge DISI engine". *Proceedings of the Combustion Institute,* **36**(3), pp. 3459–3466.

[29] Leung, K. M., Lindstedt, R. P., and Jones, W. P., 1991. "A simplified reaction mechanism for soot formation in nonpremixed flames". *Combustion and Flame,* **87**(3-4), pp. 289–305.

[30] Zhou, B., Brackmann, C., Li, Z., Aldén, M., and Bai, X. S., 2015. "Simultaneous multi-species and temperature visualization of premixed flames in the distributed reaction zone regime". *Proceedings of the Combustion Institute,* **35**(2), pp. 1409–1416.

[31] Dec, J. E., Yang, Y., and Dronniou, N., 2011. "Boosted HCCI-controlling pressure-rise rates for performance improvements using partial fuel stratification with conventional gasoline". *SAE International Journal of Engines,* **4**(1), pp. 1169–1189.

[32] Van Dam, N., Kalvakala, R. K., Boink, F., Yue, Z., and Som, S., 2019. "Sensitivity analysis of fuel physical property effects on spark ignition engine performance". Proceedings of the ASME 2019 Internal Combustion Engine Division Fall Technical Conference, Chicago, IL, October 20–23, 2019, V001T02A005, ASME. doi:`10.1115/ICEF2019-7157`.